



JPL Document D-74994

**TECHNOLOGY DEVELOPMENT
FOR EXOPLANET MISSIONS**
Technology Milestone Report

**Phase-Induced Amplitude Apodization (PIAA) Technology
Development, Milestone #2**
**Instrument Tip-Tilt Control Demonstration at
Sub-Milliarcsecond Levels**

Olivier Guyon (PI)

University of Arizona

Brian Kern (Co-I), Jet Propulsion Laboratory

Frantz Martinache (Co-I), Subaru Telescope

25 Jun 2012

National Aeronautics and Space Administration
Jet Propulsion Laboratory
California Institute of Technology
Pasadena, California

Reference herein to any specific commercial product, process, or service by trade name, trademark, manufacturer, or otherwise, does not constitute or imply its endorsement by the United States Government or the Jet Propulsion Laboratory, California Institute of Technology.

APPROVALS

Released by



Olivier Guyon, Principal Investigator
University of Arizona

JULY 17, 2012

Approved by




Peter R. Lawson
Exoplanet Exploration Program Chief Technologist, JPL

7/17/2012



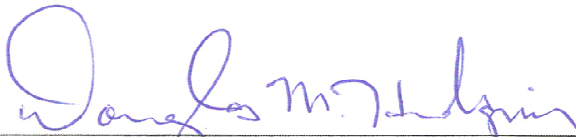
Marie Levine
Exoplanet Exploration Program Technology Manager, JPL

7/17/2012



Peter R. Lawson
Exoplanet Exploration Program Manager (Acting), JPL

7/17/2012



Douglas Hudgins
Exoplanet Exploration Program Scientist, NASA HQ

7/30/2012



Lia LaPiana
Exoplanet Exploration Program Executive, NASA HQ

7/23/2012

LIST OF ACRONYMS

CCD	charge-coupled device
CLOWFS	Coronagraphic Low-Order WaveFront Sensor
DM	deformable mirror
HCIT	High Contrast Imaging Testbed
IWA	inner working angle
JPL	Jet Propulsion Laboratory
MAM	Micro-Arcsecond Metrology
OAP	off-axis parabola
PIAA	phase-induced amplitude apodization
PSD	power spectral density (see Appendix 1)
PSF	point spread function
RMS	root mean square
sCMOS	Scientific CMOS (Complementary Metal-Oxide Semiconductor) image sensor

LIST OF ALGEBRAIC SYMBOLS

λ	wavelength of light (see also λ/D_{sky})
λ/D_{sky}	image plane distance, referenced to angles at input (Sec. 3.2)
δ_x and δ_y and δ	rms corrected residual x , y , and quadrature sum of x and y values (Sec. 3.5.7)
σ_x and σ_y and σ	mean corrected residual x , y , and quadrature sum of x and y values (Sec. 3.5.7)
ϵ_x and ϵ_y and ϵ	error in sinusoidal calibration meas., x , y , and quadrature sum of x and y (3.5.7)
Δ_x and Δ_y	actuator displacements used in CLOWFS calibration (Sec. 3.5.5)
C_x and C_y	$(I_x - I_{\text{ref}})/\Delta_x$ and $(I_y - I_{\text{ref}})/\Delta_y$ calibration of x and y actuator displacements (3.5.5)
C	$[C_x \ C_y]$ matrix of C_x and C_y column vectors (Sec. 3.5.5)
D	diameter of aperture or optical stop (see also λ/D_{sky} , Sec. 3.2), also
D	$I - I_{\text{ref}}$ column vector (Sec. 3.5.5)
f	focal length of optics (used only in definition of λ/D_{sky} , Sec 3.2), also
f	temporal frequency
i and j and k	indices to PSD calculations (Appendix 1)
I_{ref}	reference CLOWFS image (Sec. 3.5.5)
I_x and I_y	CLOWFS image after x and y actuator displacements (Sec. 3.5.5)
I	CLOWFS image (non-calibration)
m	mask of CLOWFS image pixels to be used (Secs. 3.5.1, 3.5.5), also
m	arbitrary measurement as input to PSD (Appendix 1)
M	PIAA off-axis magnification (Sec. 3.2)
P_x and P_y	PSD of x and y measurements
P	quadrature sum of P_x and P_y , implied radial (<i>i.e.</i> , total) motion PSD
$S_x, S_y, S_{1,x}, S_{1,y}, S_2, S_3$	Scaling ratios relating actuator voltages x_v, y_v to centroids at occulter x, y (3.5)
W	spectral window weighting coefficients (Appendix 1)
ξ and η	star centroid measured at science camera, in science camera pixels (Sec. 3.5.2)
x and y	star centroid x and y measurement at occulter, calibrated to λ/D_{sky} (Sec. 3.5.5)
x_v and y_v	x and y actuator voltages producing star centroid offsets, in volts (Sec. 3.5.5)
X	$[x_v \ y_v]^T$ 2-element column vector (Sec. 3.5.5)

TABLE OF CONTENTS

1. ABSTRACT.....	1
2. INTRODUCTION	1
2.1. Significance of milestone.....	1
2.2. Technical approach	2
3. EXPERIMENT CONFIGURATION	2
3.1. Optical layout.....	2
3.2. Off-axis distances.....	3
3.3. Occulter design	4
3.4. CLOWFS camera operating modes	5
3.5. Calibration and image analysis	6
3.5.1. CLOWFS image calibration.....	6
3.5.2. Science camera calibration of volts to pixels.....	7
3.5.3. Relation of science camera pixels to microns at the occulter	8
3.5.4. Relation of microns at the occulter to λ/D_{sky}	9
3.5.5. Image analysis.....	10
3.5.6. Control loop	11
3.5.7. Milestone statistics.....	11
3.6. Environment.....	11
3.6.1. In-air.....	11
3.6.2. Under vacuum.....	12
3.6.3. Artificial disturbances	14
4. MILESTONE PROCEDURES	15
5. NARRATIVE REPORT	15
5.1. Correction requirement	16
5.2. Calibration requirement	19
6. CONCLUSIONS.....	21
Appendix 1. Power Spectral Densities.....	22
Appendix 2. Error Estimates.....	23
A2.1. Random errors.....	23
A2.2. Systematic errors.....	23
A2.2.1. Errors in $S_{1,x}$ and $S_{1,y}$	23
A2.2.2. Errors in S_2	24
A2.2.3. Errors in S_3	24
A2.2.4. Total systematic errors	24
REFERENCES	25

1. ABSTRACT

This report describes the completion of Milestone 2 of the Phase-Induced Amplitude Apodization (PIAA) Technology Development experiment, funded under the NASA 2009 Technology Development for Exoplanet Missions grants. PIAA Milestone 2 is a demonstration of instrument tip/tilt control in a high-contrast coronagraph at levels relevant for a space-based exoplanet imaging mission. The milestone is a requirement to “Demonstrate $0.01 \lambda/D$ RMS pointing jitter stability and $0.003 \lambda/D$ pointing calibration at the coronagraph focal plane mask over a continuous 1-hr time period.”

This document describes the scientific relevance of tip-tilt control, the hardware used to create a Coronagraphic Low-Order WaveFront Sensor (CLOWFS) and tip-tilt control on the Jet Propulsion Lab (JPL) High Contrast Imaging Testbed (HCIT) PIAA testbed, the data analysis procedures, the relevant environmental concerns, and the results of the three Milestone 2 data runs satisfying the requirements. The milestone was met, with measured stability of approximately $0.001 \lambda/D$ and calibration to $0.0001 \lambda/D$, near $10\times$ and $30\times$ better than the requirements.

2. INTRODUCTION

This milestone demonstrates the sub-milli-arcsecond tip-tilt control required for achieving and maintaining high contrast (10^{-9} raw contrast) at small inner working angles ($< 2 \lambda/D$). While the milestone is part of an effort to advance the technology readiness of the PIAA coronagraph [1-10], both the significance of the milestone and the technical solution employed are applicable to all small inner working angle coronagraphs.

2.1. Significance of milestone

The first goal of this milestone is to demonstrate that pointing jitter at the coronagraph focal plane mask can be actively controlled to $0.01 \lambda/D$ RMS. On a 2 m diameter telescope, the $0.01 \lambda/D$ RMS pointing jitter corresponds to 0.5 milli-arcsecond (mas) at optical wavelengths, which is the radius of a Sun-like star at 10 pc distance. Achieving the RMS pointing jitter goal specified for this milestone therefore ensures that the coronagraph leak due to pointing errors is no more than the light leak due to the finite stellar angular size for telescope diameters of 2 m or more. Small inner working angle (IWA) coronagraphs, such as the PIAA coronagraph, are fundamentally limited in performance by the stellar angular size, while coronagraphs with larger IWA are insensitive to stellar angular size and can tolerate larger pointing errors. By setting the RMS pointing jitter goal at $0.01 \lambda/D$, completion of this milestone thus validates that pointing jitter can be controlled to a level such that it is not a major contributor to coronagraph light leakage, regardless of the coronagraph design employed.

The second goal of the milestone is to demonstrate that residual tip-tilt errors in the coronagraph can be calibrated to $0.003 \lambda/D$ in order to allow calibration of coronagraphic leaks due to pointing errors to a 10^{-11} contrast level on a small IWA coronagraph. While the first goal (RMS jitter) ensures that the contribution of pointing errors is below the 10^{-9} contrast level and is therefore not a significant source of photon noise, this second goal ensures that pointing errors cannot produce planet detection false positives.

The rationale for these goals is discussed in more detail in Sec. 2.2 of the Milestone 2 White Paper.

2.2. Technical approach

The approach for accomplishing this milestone is to implement and operate a dedicated sensor, the Coronagraphic Low-Order Wave-Front Sensor (CLOWFS) [11], which uses starlight otherwise rejected by the coronagraph. Using the light that falls on the central (within the coronagraph IWA) part of the focal plane mask offers two fundamental advantages over schemes relying on analysis of coronagraphic science images for pointing control:

- (1) a large number of photons is available for the measurement, allowing fast and accurate tip-tilt estimation
- (2) pointing errors can be measured before they start producing coronagraphic leaks in the science image

The milestone demonstration was performed on the existing PIAA coronagraph table which is currently in the vacuum Micro-Arcsecond Metrology (MAM) chamber at JPL. The CLOWFS implementation for this milestone closely follows the design described in the original CLOWFS publication [11]. The only significant difference is that only one defocused image is acquired by the CLOWFS camera, while the original CLOWFS assumes two images are acquired. This simplification has no impact on the CLOWFS tip-tilt functionality or performance.

3. EXPERIMENT CONFIGURATION

3.1. Optical layout

The HCIT PIAA testbed was assembled in 2009 and has been conducting high-contrast imaging experiments since [12-13]. It uses the first generation of PIAA mirrors fabricated by Axsys [7]. The implementation of a CLOWFS system required a new occulter, relay optics to deliver an image to the CLOWFS camera, and piezo actuators to perform the correction. The current testbed layout, including the components installed as part of this experiment, is shown in Fig. 1. All of the optical components are mounted on a 5'x8' optical table, which is installed in a vacuum chamber whose pressure typically reaches 10^{-6} Torr. Light is fed from a laser source outside the vacuum chamber through a single-mode fiber.

The optical path relevant to the CLOWFS system begins with an 808 nm frequency-stabilized laser diode, pigtailed to a single-mode fiber that passes via a feedthrough into the vacuum chamber. The fiber tip then illuminates a pinhole at the source location marked in Fig. 1. The source is followed by a fold mirror with piezoelectric actuators controlling its tip-tilt. The light then passes through the two PIAA mirrors, M1 and M2. The output focus of M2 is then relayed 1:1 to the occulter, where part of the PSF is reflected to the CLOWFS camera and part is transmitted to the science camera. A pair of lenses relays the light reflected off of the occulter to an image near the CLOWFS camera with a 2.5x magnification. This image is intentionally defocused before landing on the CLOWFS camera.

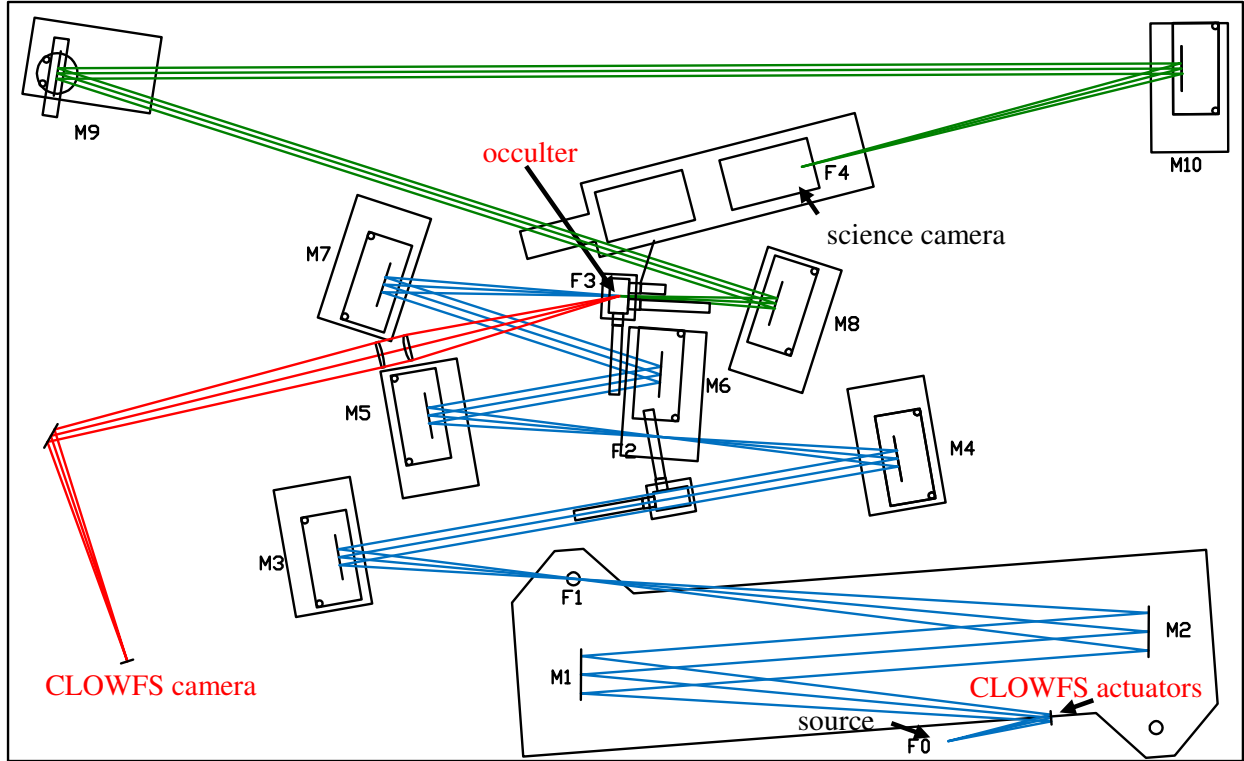


Fig. 1. Optical layout of HCIT PIAA table. The source is at the bottom-right, followed by a piezo-driven tip-tilt actuated fold mirror (“CLOWFS actuators”), then by PIAA mirrors M1 and M2, which form a source image at F1. M3 is an off-axis parabola (OAP) that collimates the light from F1 and forms an image of PIAA M2 at the postapodizer (shown here as an unmarked translation stage). OAPs M4 and M5 image and collimate the light from F1, and relay an image of the postapodizer onto the deformable mirror (DM) at M6. The OAP M7 forms a source image at the occulter (F3), which reflects part of the beam into the CLOWFS path (in red) and transmits part to the science camera path (in green, through OAP M8, flat M9, and OAP M10). The plane of the table is the x,z plane (variously oriented by defining z along the chief ray), and y is perpendicular to the table (y is parallel to gravity).

3.2. Off-axis distances

For the purposes of calibrating and controlling tip-tilt in this system, the only aspect of the PIAA mirrors that is relevant is that the images of off-axis sources receive a magnification, as measured by the location of the centroid of an off-axis image relative to the off-axis position of the source, that is not simply an effect of changing focal lengths and aperture diameters, *i.e.*, it is not a result of scaling by $f\lambda/D$. The imaging scales of the system can be understood to be defined by (f/D) at each image plane, as would typically apply to OAPs (or any powered optics which have conic surfaces), while the “additional” effects of the PIAA mirrors are encapsulated in a single multiplicative parameter M . This off-axis magnification due to the PIAA mirrors depends on the PIAA mirror prescription, as well as on the limiting stop. When this system is used for coronagraphic measurements at the science camera, a Lyot stop is inserted between the occulter and the science camera. This Lyot stop determines the off-axis magnification M for these PIAA mirrors to be $M = 2.5$, as seen by the science camera with the coronagraph fully assembled. For the

purposes of this tip-tilt experiment, all off-axis distances will be quoted as if in units of λ/D_{sky} , which is defined by:

$$\lambda/D_{\text{sky}} = \begin{cases} f\lambda/D, & \text{image planes upstream of PIAA,} \\ Mf\lambda/D, & \text{image planes downstream of PIAA,} \end{cases}$$

where $M = 2.5$, $\lambda = 808 \text{ nm}$, and $(f/D) = 16$ (approximately) at the source and at the occulter. While the expression λ/D_{sky} is dimensionless as written, which is appropriate for a telescope measuring angles on the sky, in this experiment it always has dimensions of length, as defined above. Specifically, at the source, $\lambda/D_{\text{sky}} = 13 \text{ }\mu\text{m}$, and at the occulter, $\lambda/D_{\text{sky}} = 33 \text{ }\mu\text{m}$.

This off-axis magnification, as a multiplicative factor, is essentially constant as a function of off-axis distance for the purposes of the current experiment, varying by $< 1\%$ for off-axis distances well beyond $100 \lambda/D_{\text{sky}}$.

3.3. Occulter design

The occulter used in conjunction with the CLOWFS system must prevent light within the coronagraph IWA from reaching the science focal plane, and direct starlight to the CLOWFS camera for tip-tilt measurement. As shown in Fig. 2, the occulter, when seen in transmission, blocks all light falling within $1.6 \lambda/D_{\text{sky}}$ of the optical axis. A reflective annulus directs some of the starlight onto the CLOWFS camera, while the central part of the mask is absorptive. Of the total PSF, 9% of the intensity falls on the reflective annulus, while 6% passes through the blank substrate.

As detailed in the original CLOWFS publication [11], the role of the opaque central core is to prevent most of the light in the PSF core from reaching the CLOWFS. This light is not very sensitive to tip-tilt aberrations, while the light in the steepest part of the PSF profile (falling on the reflective annulus) is most sensitive to small tip-tilt errors. The presence of this opaque core thus offers two fundamental benefits:

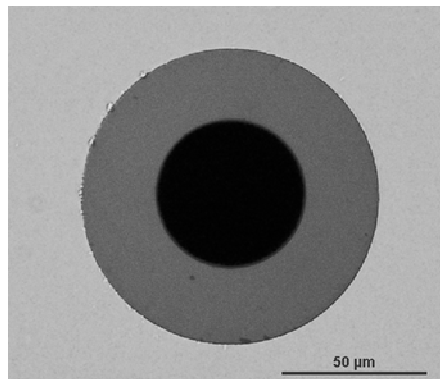


Fig. 2. Microscope image (50 \times) of CLOWFS occulter, on a glass substrate. The center portion is absorptive, the surrounding annulus is reflective, and the outer region is transmitting. The reflected portion of the beam goes to the CLOWFS camera, while the transmitted portion goes through an optional Lyot stop to the science camera. The absorptive core has a radius of $0.8 \lambda/D_{\text{sky}}$, and the reflective annulus has an outer radius of $1.6 \lambda/D_{\text{sky}}$.

- (1) A small tip-tilt error produces a macroscopic change in the light reflected to the CLOWFS camera.
- (2) The measurement is largely immune to non-common path tip-tilt errors (for example, motion of the CLOWFS camera), as the measurement is referenced to the location of the opaque spot on the focal plane mask.

The occulter shown in Fig. 2 was manufactured by lithographic techniques on a glass substrate. Several such masks were manufactured with slightly different outer radii. The mask adopted for the milestone measurements offers a $2 \lambda/D_{\text{sky}}$ coronagraph IWA.

3.4. CLOWFS camera operating modes

The CLOWFS camera currently in use is an E2V CCD39 with JPL-built supporting camera electronics. This is a split frame transfer, four-quadrant readout CCD, with 80×80 active $24 \mu\text{m}$ square pixels. The HCIT PIAA table can be operated either in air or under vacuum, and the operating environment imposes a number of specific constraints in the CLOWFS camera operation. The CLOWFS camera has a fixed frame rate, as currently implemented, of 10 Hz, but has latencies and delays that range from 0.5 s to 7 s, depending on operating mode and number of frames being collected as a batch. This frame rate is much lower than what the CCD is capable of (1000 Hz), but is limited by the software and hardware currently implemented. Rather than improving the current electronics to make use of available bandwidth, an entirely new “Scientific CMOS image sensor” (sCMOS) camera is being prepared for use as a replacement, which delivers 100 Hz (potentially up to 1.7 kHz) frame rates but has not yet been interfaced with the HCIT PIAA table.

In air, there are two CLOWFS camera modes most frequently used: a batch mode acquiring several frames at a time, and single frame mode. In batch mode, typically 100 contiguous frames are acquired at 10 Hz (taking 10 s total), followed by a 5 s latency for software overhead. In single frame mode, a single 0.1 s frame is collected and is available within milliseconds of being read out, but due to software overheads, 0.5 s pass before another frame can be stored, resulting in a latency of ms but a minimum cycle time of 0.6 s. To perform high-bandwidth corrections, the single-frame mode can be used in air, with a 1.7 Hz correction frequency.

Under vacuum, the camera fails from overheating if left powered on continuously, but can operate in a quasi-steady state indefinitely with power duty cycles below 1/4. The vacuum operating mode is then to power on the camera, typically acquire 16 frames at 10 Hz, then power down the camera, repeating the cycle once every 7 s. The images are available within approximately 2 s of readout. Of the 16 frames acquired, the first 4 are corrupted by the power-on sequence of the camera, and the remaining 12 frames (or fewer if there are read errors) are averaged to produce a single mean frame.

The CLOWFS camera is operated uncooled, and its read noise and dark current performance do not affect the work presented here in any meaningful way (an upper limit to this noise is identified in Sec. 3.6.2). To keep light levels appropriate to the fixed 10 ms exposure time, a 10^{-4} neutral density filter is inserted before the CLOWFS camera. Every frame taken with the CLOWFS camera is bias-subtracted, gain-normalized between the four amplifiers, and dark-subtracted before any additional data reduction described in this report.

3.5. Calibration and image analysis

The calibration steps of the CLOWFS system can be divided into two categories: calibration of the CLOWFS camera and actuators to allow closed-loop correction in terms of actuator voltages, and determination of a scale factor relating volts to λ/D_{sky} measures. The CLOWFS tip-tilt corrections do not rely on the scaling of voltages to λ/D_{sky} , and so require only the first category to operate. A schematic diagram of the different calibration steps is shown in Fig. 3.

The scaling relationships are quantified as two constants, S_x and S_y . These constants relate the actuator voltages x_V and y_V to centroids at the occulter, x and y (measured in λ/D_{sky}), via

$$x = S_x x_V$$

$$y = S_y y_V$$

The scaling constants themselves are broken into individually determined factors,

$$S_x = S_{1,x} S_2 S_3$$

$$S_y = S_{1,y} S_2 S_3$$

where $S_{1,x}$, $S_{1,y}$, S_2 and S_3 are defined in the sections that follow.

3.5.1. CLOWFS image calibration

The CLOWFS camera and actuator calibration involves only empirical correlations between actuator motions and observed changes in CLOWFS images, with no consideration given to *a priori* calculations of the optical properties of the system. The procedure is to acquire, in principle, three images: a reference image, an image taken after moving only the x actuator, and an image taken after moving only the y

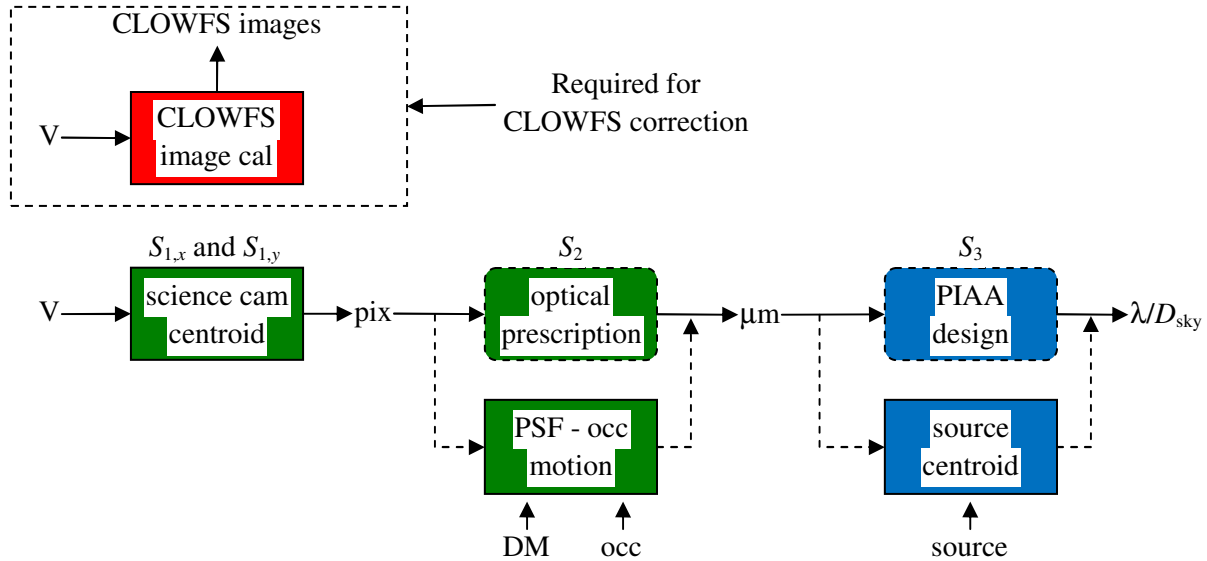


Fig. 3. Schematic showing relationships between calibration steps. The “CLOWFS image cal” step (top-left, in red) is the only step that is relevant for tip-tilt correction; the remaining steps are required to scale residual offsets to λ/D_{sky} . The rounded boxes with dashed borders represent non-measured quantities, and the dashed flow-lines denote verification steps which are used to establish error estimates but are not included in the direct calibration. The steps and inputs involving the focal plane occulter use the abbreviation “occ.” The colors relate to the regions of Fig. 1 where the relationships are established.

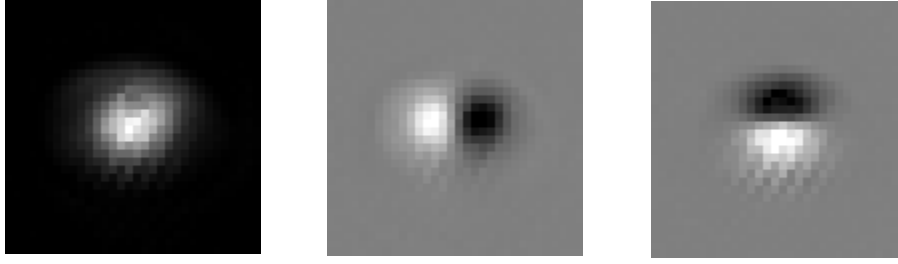


Fig. 4. (LEFT) CLOWFS reference image, (CENTER) CLOWFS x -calibration difference image, (RIGHT) CLOWFS y -calibration difference image, both calibrations using approximately $50 \times 10^{-3} \lambda/D_{\text{sky}}$ offsets. The intensity scale on the center and right panels is $\pm 0.04 \times$ the full scale on the left panel. These images were the calibration for Milestone run #1.

actuator. Every image, during calibration and during correction, is normalized by total counts in a photometric aperture 12 pixels in radius. The normalized reference image is subtracted from every normalized image taken during calibration and during correction; all data is considered to be differential with respect to the reference image. The CLOWFS x - and y -calibration difference images, examples of which are shown in Fig. 4, form a two-element basis used to reduce all subsequent difference images into x and y offsets (scalars), which are the error signals for closed-loop correction. Because the relevant region of the image is small compared to the entire CCD field, a mask is applied, with radius 12 pixels, to exclude the “zero” portions of the image from further analysis. This mask is identical to the photometric aperture used for normalization.

Using the image analysis described in Section 3.5.5 below, all subsequent images used in normal operation of the CLOWFS camera (*i.e.*, non-calibration images) are reduced to a pair of x -actuator and y -actuator voltages, which can be considered an error signal relative to the configuration of the reference image. This calibration alone is enough to perform closed-loop corrections, in terms of actuator voltages. This CLOWFS image calibration is repeated every milestone run.

3.5.2. Science camera calibration of volts to pixels

The science camera is used to establish a correlation between piezo actuator voltages and centroid motion of the PSF at the occulter, measured in science camera pixels. This is quantified by the scaling constants $S_{1,x}$ and $S_{1,y}$. The occulter is removed, so that the science camera is directly imaging the occulting plane. By applying sinusoidal voltage patterns to the x and y actuators, simultaneously at two different temporal frequencies, and measuring the centroid motion at the science camera, a relationship between volts and science camera pixels is established. These centroid measurements are shown in Fig. 5, with ξ and η denoting the science camera pixel axes (x approximately aligned with ξ , and y with η). The relationship between volts and pixels is different for the x actuator than for the y actuator, because the piezo actuators themselves have different gains. There was no accommodation given to cross-terms in the analysis of the centroid data, as would be expected by a misalignment of the actuator axes and the science camera pixel axes (certainly present at some level). This is readily apparent in the ξ residuals in Fig. 5, which show the temporal frequency of the y actuator sinusoid, with about 2.7% of the η amplitude. The magnitude of this term does not affect the calibration enough to merit a more complicated treatment (residuals in Fig. 5 have a different vertical scale than the original measurements).

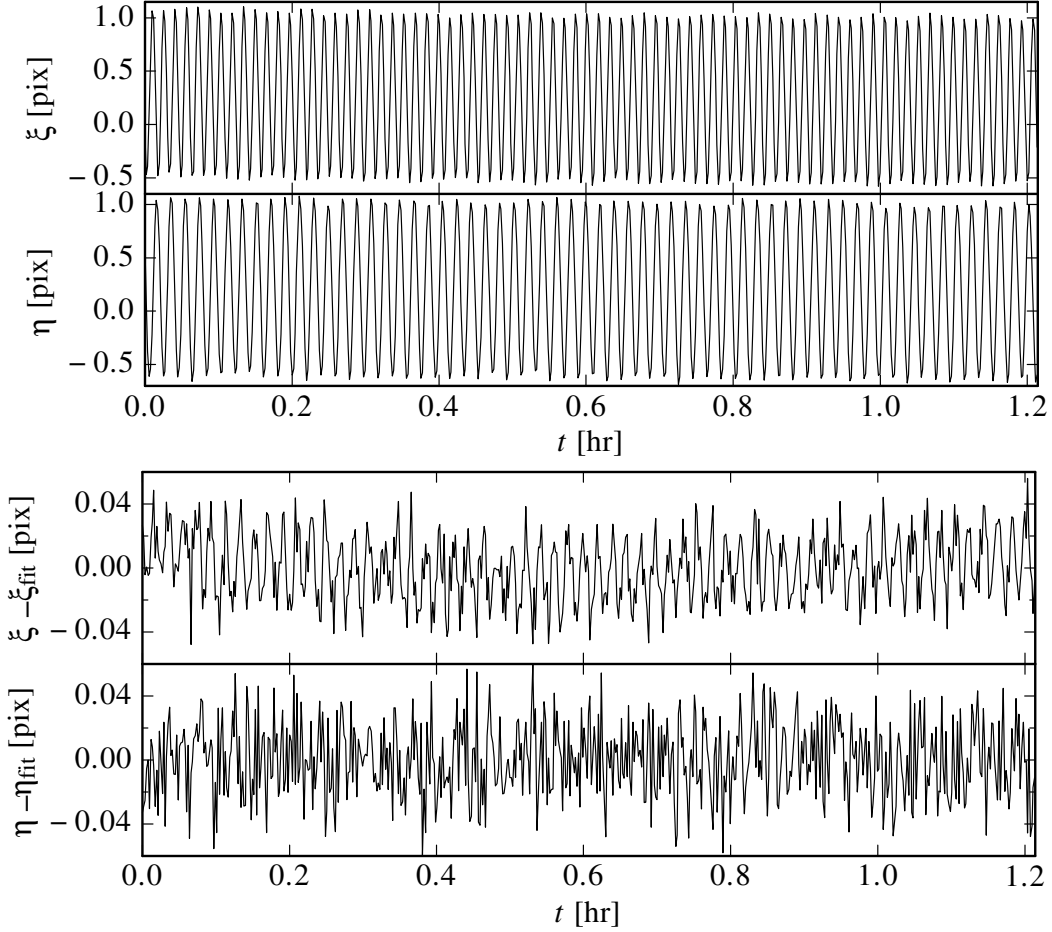


Fig. 5. (TOP) Science camera centroid x - and y -calibration of CLOWFS actuator, and (BOTTOM) residuals from fit. The data are ξ - and η -centroids of unocculted images taken with the science camera, while applying 2 V sinusoids at two different temporal frequencies to the x and y CLOWFS actuators. The data are fitted to the sum of a first-order polynomial and a sinusoid of unknown amplitude and phase (frequency is not fit). The residual plots are displayed with a 15 \times finer vertical scale than the centroid data. The zero-points of ξ and η in the top panel are nominal pixel boundaries, which have arbitrary offsets with respect to the initial position of the star centroid.

3.5.3. Relation of science camera pixels to microns at the occulter

There are two techniques used to determine the relationship between pixels at the science camera and microns at the occulter, the first of which determines S_2 and the second of which estimates the errors on S_2 (an upper limit to the uncertainty). The first technique uses the *a priori* defined specification of the CCD and the optical prescription of the PIAA coronagraph. The second technique is a dynamic empirical technique involving measurements with the science camera.

The first technique to measure S_2 , labeled “optical prescription” in Fig. 3, involves just two numbers. The two OAPs that image the occulter onto the science camera have a nominal magnification of 2.5, and the science camera CCD pixels are nominally 13 μm square, implying $S_2 = 5.2 \mu\text{m}/\text{pix}$ at the occulter. This number is used in the analysis that follows.

The second technique also measures S_2 , but is used only to estimate errors on S_2 . This is labeled “PSF – occ motion” in Fig. 3. The technique is to take a science camera image with the occulter in, to move both the PSF and the occulter to recreate the same science camera image shifted by some number of pixels. The occulter motion is controlled by an encoded stepper motor, so the encoder can then be used to determine the distance the occulter moved, corresponding to a number of pixels of motion at the science camera.

This second technique for S_2 works best if the occulted PSF is morphologically unchanged except for location on the science camera. The CLOWFS actuators are not appropriate to offset the PSF in this way, as the PIAA optics create a distorted off-axis PSF when the actuators move by substantial amounts. Rather, a set of piezo actuators that control tip-tilt of the DM mount are used for this calibration; these actuators are not used in any other part of this experiment, but they do allow for simple translation of the PSF at the occulter, with negligible change to the PSF morphology.

The scaling from the first technique for S_2 , using a priori knowledge, is used for all image analysis, while the results from the second technique appear in the error analysis in Appendix 2.

3.5.4. Relation of microns at the occulter to λ/D_{sky}

There are two techniques used to determine S_3 , the relationship between microns at the occulter and λ/D_{sky} . The first S_3 technique is to use the nominal optical prescription, and the PIAA off-axis magnification, to calculate $Mf\lambda/D$. The second S_3 technique uses a dynamic empirical technique to measure relevant quantities at the science camera. Just as in the previous section, the *a priori* knowledge (first technique) determines S_3 as used in the analysis, while the second technique provides an error estimate.

The first S_3 technique is labeled “PIAA prescription” in Fig. 3. The optical prescription gives $f\lambda/D$, and the PIAA off-axis magnification (see Sec. 3.2) is $M = 2.5$, giving $\lambda/D_{\text{sky}} = 33 \mu\text{m}$ at the occulter. This number is used in the image analysis to follow.

The second S_3 technique, labeled “source centroid” in Fig. 3, begins by offsetting the source by a known distance, using an encoded motor to translate the source (not the piezo-controlled tip-tilt of a fold mirror), and measuring the centroid motion at the science camera, with the Lyot stop in. This gives a relationship between microns of motion at the source and pixels of motion at the science camera, which can be converted (using the result of 3.5.3) to relate microns of motion at the source to microns of motion at the occulter, which is a measurement of $(Mf\lambda/D)_{\text{occ}} / (f\lambda/D)_{\text{src}}$. Nominally, $(f/D)_{\text{occ}} = (f/D)_{\text{src}}$, and of course λ is the same everywhere, so this measurement yields a measurement of M . f/D is measured separately by moving the camera longitudinally between a source image plane and a pupil image plane, using the encoder on the camera motion stage to know the distance, and measuring the pupil image diameter in pixels at the science camera, with the Lyot stop out. Using the known pixel size, this establishes f/D at the camera via empirical measurements. The magnification between the camera and the occulter was established as 2.5 in Sec. 3.5.3 and A2.2.2, so $(f/D)_{\text{cam}} = 2.5 (f/D)_{\text{occ}}$. Using the specified laser wavelength (measured by a spectrometer to be accurate to $< 0.1\%$), this yields a measurement of $Mf\lambda/D$ at the occulter, having assumed the science camera pixel size and $(f/D)_{\text{occ}} = (f/D)_{\text{src}}$.

The details of the use of the results from the second technique’s error estimates appear in Appendix 2.

3.5.5. Image analysis

The calibration difference images are $C_x = (I_x - I_{\text{ref}})/\Delta_x$, and $C_y = (I_y - I_{\text{ref}})/\Delta_y$, where Δ_x and Δ_y are the x and y actuator motion, in V, used to construct the calibration difference images, as described in Section 3.5.1. C_x and C_y have dimensions of normalized intensity per volt. A linear model of actuator motion would then predict, for an arbitrary choice of actuator commands x_V and y_V , a difference image, $D = I - I_{\text{ref}}$, according to

$$D = x_V C_x + y_V C_y,$$

which is rewritten in matrix notation as

$$D = CX$$

where D is a vector of individual normalized intensities per pixel in the difference image, C is a matrix with two columns, a column of values per pixel from C_x , and a column of values per pixel from C_y , and X is a two-element vector containing x_V and y_V . The two-dimensional nature of each image (D , C_x , and C_y) is not relevant beyond ensuring that the indexing of pixels is the same between images, *i.e.*, any linear operations operate on the same two-dimensional locations in each image. Consistent pixel registration is relevant, while identifying separate pixels as being neighbors or not, for example, is not relevant.

The mask m describing the region of interest (as described in Section 3.5.1) is a set of pixels, in this case, 437 pixels. Restricting the calculations to these pixels implies that D is a 437-element column vector, C is a 437×2 matrix, and X is a 2-element column vector.

For each subsequent image, using its associated difference image $D = I - I_{\text{ref}}$, we solve $D = CX$ for X in a linear least-squares sense, using

$$X = (C^T C)^{-1} C^T D$$

By construction, C_x and C_y are nearly orthogonal, so $C^T C$ is well conditioned and the inversion is straightforward. This treatment implies identical weighting for each pixel in the image plane. While it would be preferable to weight them inversely to the expected measurement noise per pixel, in practice, the measurement noise is small compared to any relevant signals in question (see Section 3.6.2), and the complication of nonuniform weighting was not necessary.

One benefit of all image analysis being differential is that this linear analysis will be unaffected by errors in bias subtraction, dark subtraction, and flat-fielding.

Once each difference image is reduced to x_V and y_V as above, these error signals are translated into λ/D_{sky} units, as established in sections 3.5.2-3.5.4, and denoted simply x and y . In addition to interpreting x and y as the actuator motions that would translate the stellar image from the reference image to the observed image, x and y can also be interpreted as the x and y star centroids at the occulter, measured in λ/D_{sky} , assuming the applicability of linearity in the measurements. This linearity assumption is tested, in part, by the milestone calibration verification requirement, described in Sec. 5.2, where the agreement is found to be excellent.

3.5.6. Control loop

An integrator control law was used, with an integrator gain equal to 1. In the simplest terms, new voltage = old voltage – 1× measured offset. Under vacuum (see Secs. 3.4 and 3.6.2), sensing was done once every 7 s, using (at most) 12 frames of 0.1 s each, all averaged for a single measurement. The duty cycle of exposure time to sensing period is then $1.2 / 7 = 0.17$. In a single sensing cycle, the time lag between the end of the exposure of the last frame and the application of a correction was approximately 0.5 s (this number was not well characterized). The temporal delay between sensing and measurement is thus much shorter than the time span between measurements.

The CLOWFS response is only linear if the tip-tilt error is within $\sim 300 \times 10^{-3} \lambda / D_{\text{sky}}$ (the exact level depends on the degree of nonlinearity tolerated), as described in Ref. 11. The results described in this report were all acquired within this range, but the conclusions from these results should not be extrapolated beyond the linearity domain. Linearity impacts the CLOWFS performance on two levels:

(1) it may be difficult to close the CLOWFS control loop if the initial tip-tilt value is well outside the linearity range. Laboratory and on-sky experience at the Subaru Telescope has shown that the CLOWFS loop converges with an initial error as large as $0.5 \lambda / D_{\text{sky}}$.

(2) non-linearities may affect the interpretation of the closed loop data. In this report, the tip-tilt residuals after correction are too small ($\sim 10^{-3} \lambda / D_{\text{sky}}$) for such non-linearity to be noticeable, but care must be taken when extrapolating these results and the inferred error transfer function to large input error levels.

3.5.7. Milestone statistics

The three statistics that are used to satisfy the milestone requirements are an rms value, to measure the size of the tip-tilt residuals (*i.e.*, jitter), a mean, to verify that the average offset is acceptably small, and the measured error in a sinusoidal calibration signal. The rms values are $\sigma_x = \langle x^2 \rangle^{1/2}$, $\sigma_y = \langle y^2 \rangle^{1/2}$, and $\sigma = \langle x^2 + y^2 \rangle^{1/2}$, where $\langle \dots \rangle$ is a mean over an entire sequence. Note that the rms values are not standard deviations, in that they do not subtract the mean x and y values. The mean values are $\delta_x = \langle x \rangle$, $\delta_y = \langle y \rangle$, and $\delta = (\langle x \rangle^2 + \langle y \rangle^2)^{1/2}$. The measurement of x and y sinusoidal calibration signals, of known amplitudes, will have errors (difference between known and measured amplitudes) ϵ_x and ϵ_y , and a total error $\epsilon = (\epsilon_x^2 + \epsilon_y^2)^{1/2}$. Both the δ and ϵ statistics are considered calibration residuals.

3.6. Environment

3.6.1. In-air

When operating in air, the uncorrected x and y power spectral densities were measured (the definition of power spectral density, along with the window used in analysis and smoothing of the plots, used here is described in Appendix 1), and their sum is shown in Fig. 6. It is adequately represented as a broken power law, $P \propto f^n$, with indices $n = 0$ for $f < 0.03$ Hz, and $n = -3$ for $f > 0.03$ Hz. The spectrum shown in Fig. 6 is just one example, but on other occasions, while the low-frequency power level and knee frequency were similar, the high-frequency power law index was shallower, $n \sim -2$, implying more high-frequency power and correspondingly larger residuals after closed-loop correction. The reasons for the different in-air behaviors have not been investigated.

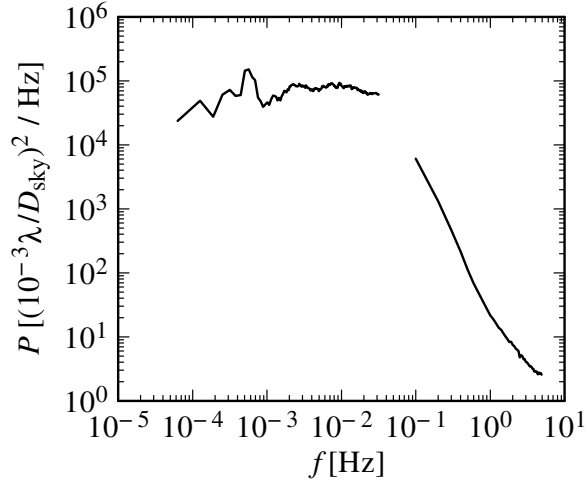


Fig. 6. Power spectral density of uncorrected CLOWFS measurements in air, with x and y powers summed. The data were acquired in sets of 100 images taken at 10 Hz, followed by a 7 s delay before acquiring the next set of 100 images. The PSD below 0.03 Hz is calculated between sets of images, while the PSD above 0.1 Hz is an average of PSDs from sets of 100 images. The break in the frequency coverage from 0.03 Hz to 0.1 Hz is indicative of the pause between sets of 100 images. The plot is smoothed as described in Appendix 1.

The uncorrected in-air rms motion (quadrature sum of x and y) shown in Fig. 6 over a ~ 4.5 hour time span is approximately $40 \times 10^{-3} \lambda / D_{\text{sky}}$, larger than the milestone threshold of $10 \times 10^{-3} \lambda / D_{\text{sky}}$ by a factor of 4. The expected residual level after closed-loop correction, with a correction every 0.6 s, would be in the neighborhood of $20 \times 10^{-3} \lambda / D_{\text{sky}}$, which depends strongly on the high-frequency power-law index, and on the closed-loop gain at frequencies above the unity-gain frequency, $1/(2\pi \times 0.6 \text{ s}) = 0.27 \text{ Hz}$, the frequency beyond which existing power is amplified.

The data shown in Fig. 6 were acquired over a longer time interval than the milestone requirement (4.5 hours as compared to a 1 hour minimum requirement), and reducing the time interval would reduce the rms image motion. However, because the power spectral density is relatively flat at low frequencies, the rms does not decrease significantly until the time interval decreases to below 100 s (*i.e.*, $\int P df$ from 0 to 10^{-2} Hz is small compared to $\int P df$ from 10^{-2} Hz to ∞). For time intervals relevant to the milestone requirement, the uncorrected rms will always be around 40×10^{-3} .

In any case, the only road to achieve milestone levels in this in-air environment is to increase the correction bandwidth, which is limited by the camera readout rate. As stated in Section 3.4, this approach has been postponed until a new camera system is integrated into the coronagraph.

3.6.2. Under vacuum

The image motion under vacuum is far less than that in air. A 12-hour sample of uncorrected CLOWFS measurements, taken under vacuum with CLOWFS camera images sampled once every 7 s, is shown in Fig. 7. What is immediately apparent about the y measurements (y is vertical) is that they are dominated by a linear drift term. The origin of this drift is not known, and does not correlate with temperature. For the purposes of describing the power spectral density of the uncorrected CLOWFS measurements under

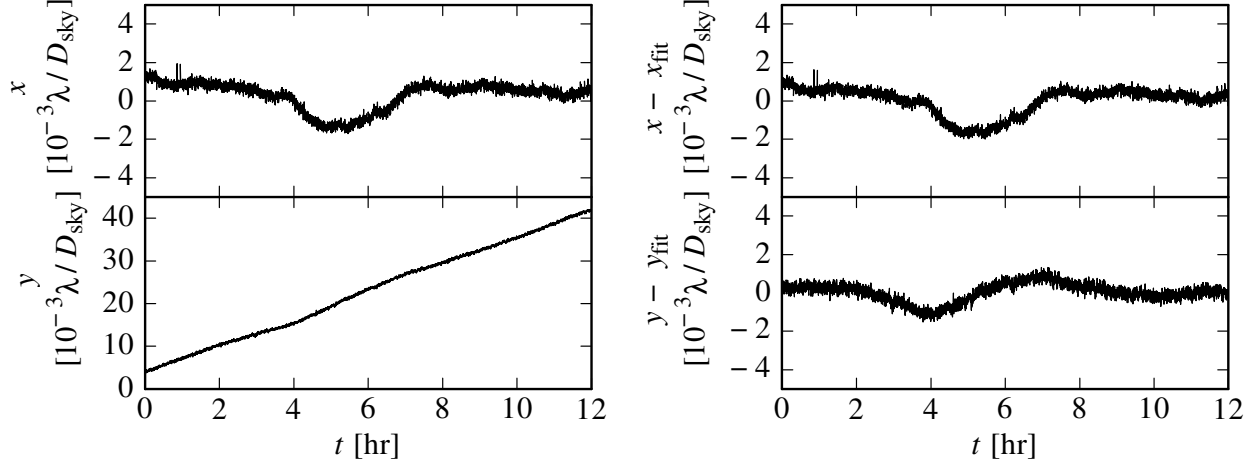


Fig. 7. (LEFT) Uncorrected CLOWFS measurements, (RIGHT) uncorrected CLOWFS drift-subtracted (first-order polynomial) residuals, taken under vacuum with no disturbances added.

vacuum, it is worthwhile to examine a drift-subtracted time series of measurements, shown in the right-hand panel of Fig. 7. A first-order polynomial is subtracted to remove drift. The drift-subtracted rms motion (quadrature sum of x and y) over the entire 12-hour span is $0.75 \times 10^{-3} \lambda / D_{\text{sky}}$, dominated by low-frequency power. This is far below the milestone requirement of $10 \times 10^{-3} \lambda / D_{\text{sky}}$, without applying any correction.

The power spectral density of the uncorrected drift-subtracted CLOWFS motion under vacuum is shown in Fig. 8. What is apparent, beyond the dominance of low-frequency power, is that the high-frequency power appears to have reached an asymptote, likely a white noise level due to measurement noise. This is a comfortably low noise level, at approximately $0.5 \times (10^{-3} \lambda / D_{\text{sky}})^2 / \text{Hz}$. At this level, the rms noise contribution integrated over all frequencies up to the Nyquist frequency of $(1/14) \text{ Hz}$, is only $0.2 \times 10^{-3} \lambda / D_{\text{sky}}$.

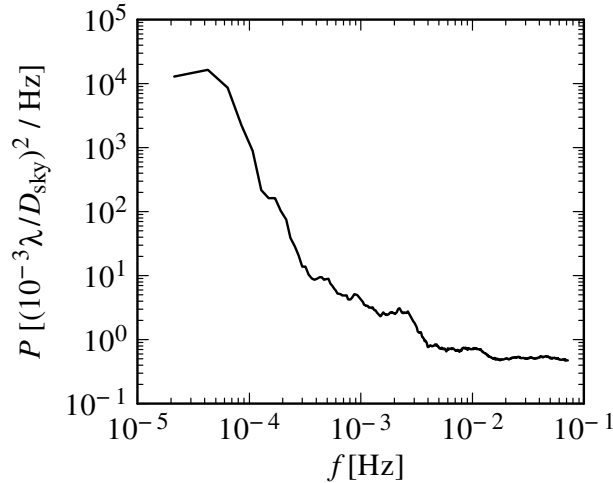


Fig. 8. Power spectral density of uncorrected drift-subtracted residuals in right-hand panel of Fig. 7, with x and y powers summed. The flat portion of the spectrum at the highest frequencies is indicative of a white measurement noise component, at a level of approximately $0.5 \times (10^{-3} \lambda / D_{\text{sky}})^2 / \text{Hz}$, corresponding approximately to $0.2 \times 10^{-3} \lambda / D_{\text{sky}}$ rms noise in the time sequence of Fig. 7. The plot is smoothed as described in Appendix 1.

3.6.3. Artificial disturbances

Given the low “background” CLOWFS motion power under vacuum, the approach taken here to demonstrate the Milestone 2 performance is to operate under vacuum and introduce disturbances through the same actuators used to implement the CLOWFS correction. The power spectral density of these disturbances is chosen to mimic the in-air motion broken power-law shape, with a knee frequency chosen to be (1/7200) Hz. This particular knee frequency was chosen for two reasons, first to be relevant to the time interval appropriate to the milestone demonstration ($1250 \times 7 \text{ s} = 8750 \text{ s}$), and second to be higher than the observed in-air knee frequency (0.03 Hz) scaled by the expected future CLOWFS operating frequency (100 Hz) divided by the current operating frequency (1/7 Hz), which comes to (1/23000) Hz. The implication is that after upgrading to the new CLOWFS camera, the in-air corrected performance should be better than the milestone performance demonstrated here under vacuum with added disturbances.

The overall level of added disturbances was chosen to deliver around $90 \times 10^{-3} \lambda/D_{\text{sky}}$ rms in a two-hour interval. This corresponds to a 5 mas pointing jitter for a 2 m telescope in visible light, comparable to the pointing jitter achieved in orbit on existing observatories (HST, Kepler and Spitzer). The level of added disturbance is therefore representative of what may be experienced on a space telescope which is otherwise not highly optimized for pointing jitter mitigation. We however note that the frequency distribution of the pointing error is very specific to the telescope and spacecraft design (reaction wheel speed and damping), and our added disturbance power spectrum (described below) may thus be quite different from what would be experienced by the telescope.

The power-law indices chosen for the disturbances were $n = 0$ and $n = -3$ for frequencies below and above the knee, similar to what was seen in Fig. 6. The disturbances were calculated and applied at intervals of 3.5 s, two samples for every one CLOWFS camera frame and correction iteration (once every 7 s). When no corrections are applied, the x and y measurements are measurements of the disturbances alone. Specifically, they are the sum of the ambient under-vacuum disturbances (Fig. 8) and the artificial disturbances, but in every case the ambient under-vacuum disturbances are negligible compared to the artificial disturbances.

Each pre-calculated sequence of disturbances can be applied to the system as many times as desired. Specifically, a sequence of disturbances can be applied while simultaneously applying corrections, and then the same sequence can be applied without also applying corrections. The same image analysis (Sec. 3.5.5) is performed whether corrections are applied or not, ensuring that the differences between measurements of corrected and uncorrected sequences using the same disturbances do represent the effect of the corrections, to the level of repeatability of the disturbances. The measured repeatability between two 2-hour sequences (separated by 6.5 hours) is $10^{-3} \lambda/D_{\text{sky}}$ rms, compared to the $90 \times 10^{-3} \lambda/D_{\text{sky}}$ rms overall disturbance level. This $10^{-3} \lambda/D_{\text{sky}}$ level is smaller than that shown in Fig. 7 (taken under vacuum with no disturbances added) without removing drift ($2 \times 10^{-3} \lambda/D_{\text{sky}}$ rms over 2 hours) but larger than that after removing drift ($0.3 \times 10^{-3} \lambda/D_{\text{sky}}$ rms over 2 hours). If a disturbance sequence is repeated on a timescale over which the drift is correlated (at least 12 hours, see Fig. 7), the drift should largely vanish from to the $10^{-3} \lambda/D_{\text{sky}}$ repeatability measurement, implying that the $10^{-3} \lambda/D_{\text{sky}}$ repeatability has a small contribution from the underlying vacuum disturbances (which, of course, do not repeat).

4. MILESTONE PROCEDURES

The success criteria for the milestone are those defined in the white paper, repeated here, with only the section numbers changed to match the numbering in this document.

4.1. The duration of the experiment for each of the measurements should be at least 1 hr and correspond to at least 1000 CLOWFS samples. Both constraints must be satisfied: the measurement should therefore last more than 1 hr if the frame rate is insufficient to obtain 1000 samples within 1 hr, and the measurement will consist of more than 1000 samples if the frame rate is sufficiently fast to obtain the 1000 samples in less than 1 hr.

Rationale: *This ensures that a sufficiently large number of measurement points are used toward computing the jitter and calibration residuals.*

4.2. A residual jitter of $0.01 \lambda/D$ or smaller shall be achieved as defined in Sec. 3.5.7. This requirement is on the radial jitter value: the quadratic sum of the jitter in x and y must be $0.01 \lambda/D$ or smaller.

Rationale: *This provides evidence that the coronagraph leak due to tip-tilt errors is smaller than the contribution of stellar angular size.*

4.3. A calibration residual of $0.003 \lambda/D$ or smaller shall be achieved as defined in Sec. 3.5.7. This requirement is on the radial calibration residual value: the quadratic sum of the calibration residual in x and y must be $0.003 \lambda/D$ or smaller.

Rationale: *This ensures that calibration of tip-tilt errors is sufficient to recover planets 10 times fainter than the 1×10^{-9} contrast raw scattered light due to stellar angular size, zodiacal light and exozodiacal light.*

4.4. Elements 4.1 – 4.3 must be satisfied on three separate occasions with a reset of the CLOWFS (discarding calibration and re-calibrating the CLOWFS) between each demonstration.

Rationale: *This provides evidence of the repeatability of the contrast demonstration. The CLOWFS reset between data sets ensures that the three data sets can be considered as independent and do not represent an unusually good configuration that cannot be reproduced. There is no required interval between demonstrations; subsequent demonstrations can begin as soon as prior demonstrations have ended.*

5. NARRATIVE REPORT

The milestone data were recorded on three runs between March 22 and 23, 2012, all under vacuum. Each run comprised four parts: a calibration of x and y actuator motions relative to CLOWFS images, a 1250-iteration sequence with the correction loop operating and a predetermined sequence of disturbances applied, a 1250-iteration sequence with no correction and the same sequence of disturbances applied, and a 625-iteration sequence of uncorrected measurements of small-amplitude sinusoids to verify sensitivity thresholds. After the calibration, all CLOWFS data are acquired at a rate of 1 iteration per 7 s, so 1250 iterations lasts nearly 2.5 hours, and the entire set of $1250 + 1250 + 625$ iterations lasted just over 6 hours per milestone run. A schematic representation of the activities in each milestone run, and the statistics produced, is shown in Fig. 9.

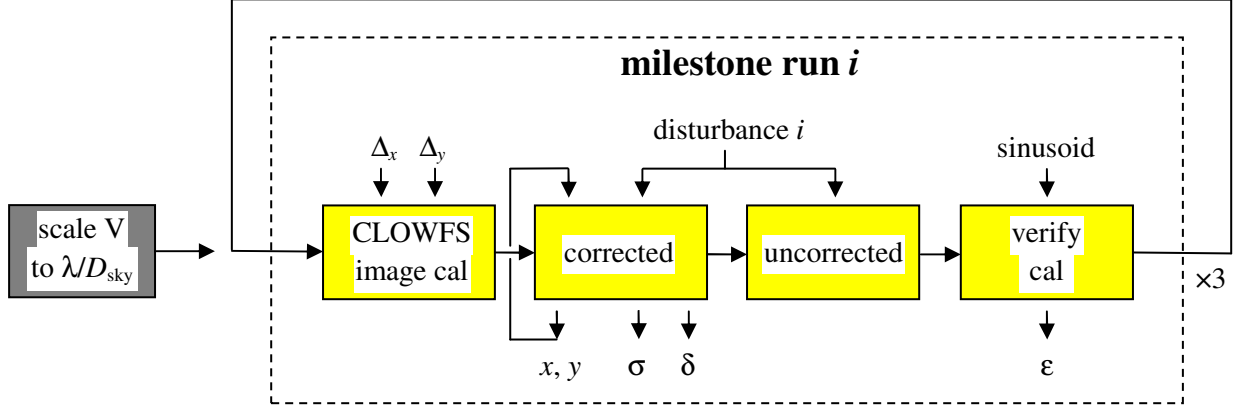


Fig. 9. Schematic showing sequence of calibration and measurement activities, and the production of milestone statistics. The first scaling step (in gray) happens only once. The milestone runs are repeated three times, producing a value of σ , δ , and ϵ for each run. Each milestone run has a different sequence of disturbances, but each sequence is repeated twice in a single milestone run, once applying corrections and once with no corrections applied.

The choice of 1250 iterations per corrected milestone sequence contains a margin in excess of the requirement of 1000 iterations, and at least 1 hour. Since the disturbance power is dominated by low temporal frequencies, longer time intervals should present more challenging conditions, so the choice of 1250 iterations rather than the minimum 1000 iterations does not bias the results to lower residuals.

The characteristics of the three milestone data runs are very similar. The disturbances added were different realizations of the same underlying temporal power spectrum, so while the specific time sequences of the disturbances differ, their power spectra are all, by construction, very similar.

5.1. Correction requirement

The corrected and uncorrected x and y measurements for the three milestone runs are shown in Fig. 10. Because the corrected measurements are so much smaller than the uncorrected measurements, Fig. 11 contains only the corrected measurements, with the vertical axis scaled appropriately. The time axes on each of these plots should be interpreted as time since the start of each disturbance sequence, and imply synchronicity in the applied disturbances between the uncorrected and corrected sequences, but the corrected and uncorrected data were not concurrent. To restate, one entire corrected sequence is obtained and plotted versus time, then the disturbances are repeated and the uncorrected sequence is obtained and overlaid on the same plot. At any given time t in one plot, the uncorrected and corrected data points at that time had the same disturbance applied, but the uncorrected data point was acquired 2.5 hours after the corrected data point, for example.

The correction requirement of the milestone states that the rms total motion (quadrature sum of x and y measurements) after correction should be less than $10 \times 10^{-3} \lambda/D_{\text{sky}}$. The uncorrected sequences show disturbances at approximately $9 \times$ this value, specifically $\sigma = 87, 87, \text{ and } 95 \times 10^{-3} \lambda/D_{\text{sky}}$. For the corrected sequences, the rms total motion was $\sigma = 1.07, 1.10, \text{ and } 1.05 \times 10^{-3} \lambda/D_{\text{sky}}$, more than a factor of $9 \times$ better than the milestone requirement.

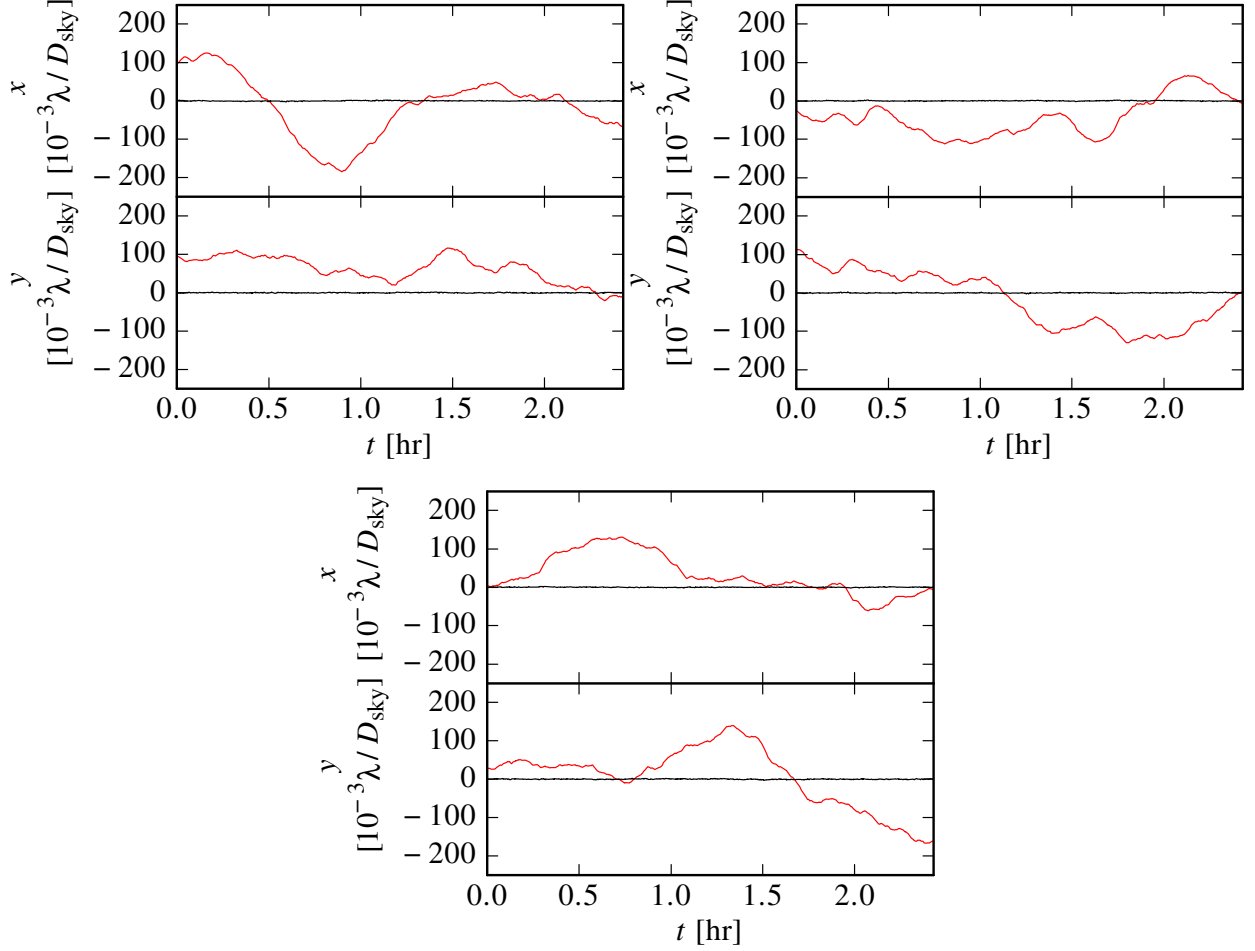


Fig. 10. (TOP LEFT) Milestone 2 CLOWFS data run #1, (TOP RIGHT) Milestone 2 CLOWFS data run #2, (BOTTOM) Milestone 2 CLOWFS data run #3. All runs are performed in vacuum, with injected disturbances. Each plot is an overlay of two sequences experiencing the same disturbances, with black lines representing corrected measurements, and red lines representing uncorrected measurements. Iterations are separated by 7 s, and each sequence comprises 1250 iterations (*i.e.*, 1250 corrected iterations and 1250 uncorrected iterations). The quadrature sums of x and y standard deviations are 87 , 87 , and $95 \times 10^{-3} \lambda/D_{\text{sky}}$ for the uncorrected data in the three runs.

No particular attention was paid to the quality of the match between the disturbances introduced and the corresponding uncorrected measurements. The only point that is relevant for this demonstration is the power spectral density of the uncorrected measurements versus the corrected measurements, and the repeatability of the disturbances between the two sequences. For comparison, a representative 2.5-hour interval from the left panel of Fig. 7 (uncorrected measurements with no disturbances) would be dominated by the linear drift term, which would contribute approximately $8 \times 10^{-3} \lambda/D_{\text{sky}}$ to the uncorrected measurements. This number is small compared to a representative uncorrected peak-to-valley measurement of $\sim 200 \times 10^{-3} \lambda/D_{\text{sky}}$.

The power spectral densities of the uncorrected and corrected sequences are shown in Fig. 12. The differences in the power spectra between the three uncorrected runs are small relative to the differences

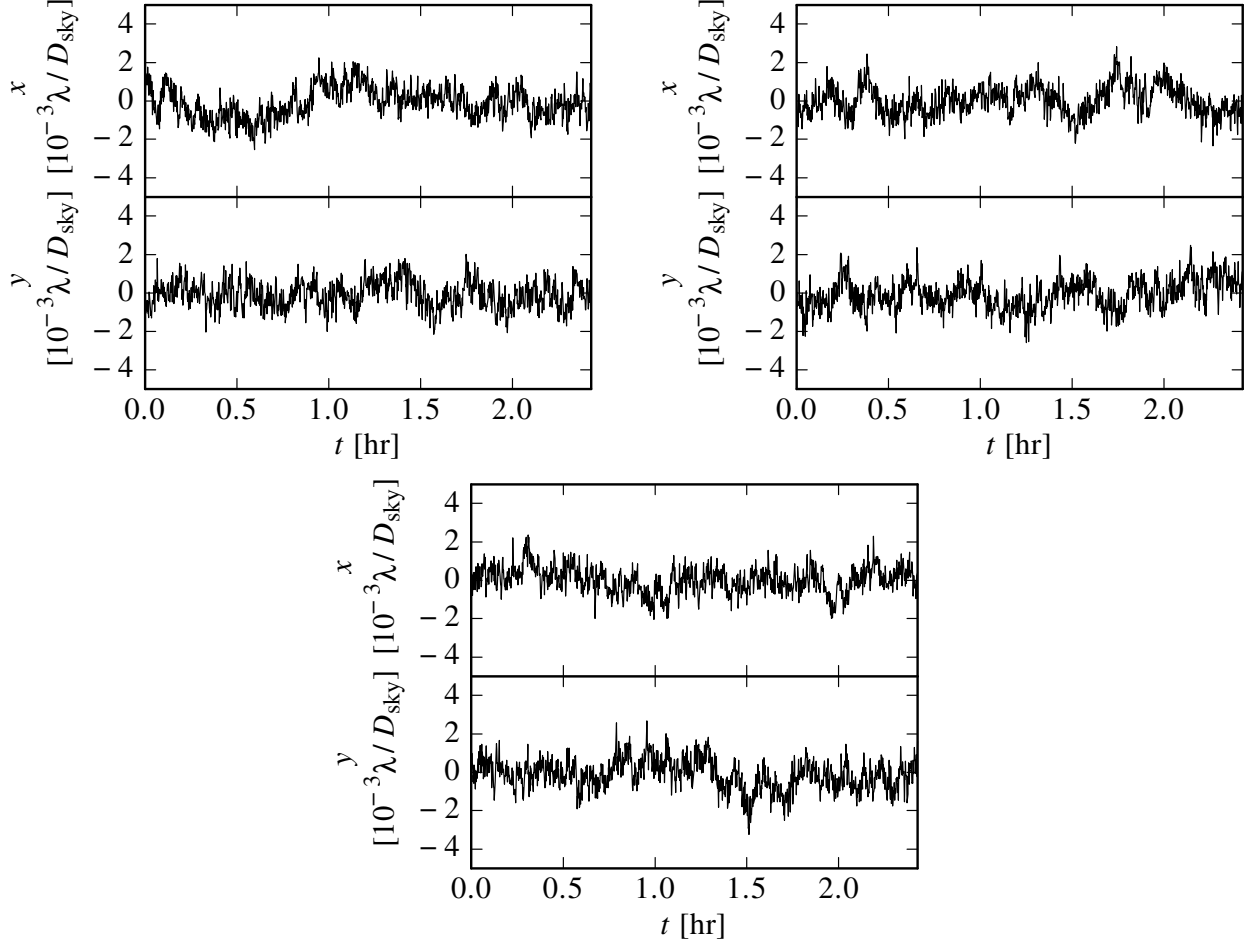


Fig. 11. Same data in each panel as in Fig. 10, but only corrected CLOWFS data are shown, with vertical scale adjusted by $50\times$ relative to Fig. 10. The quadrature sums of x and y rms residuals are 1.07 , 1.10 , and $1.05 \times 10^{-3} \lambda D_{\text{sky}}$ for the three runs, well under the Milestone 2 requirement of $10 \times 10^{-3} \lambda D_{\text{sky}}$.

between uncorrected and corrected sequences. None of the measurements reaches the asymptotic white noise level seen in Fig. 8, at $0.5 \times (10^{-3} \lambda D_{\text{sky}})^2 / \text{Hz}$, justifying the statement that measurement noise plays no significant role in the residual tip-tilt measurements.

For a given milestone run (*i.e.*, given identical disturbances), the uncorrected and corrected power spectral densities should be related by the square of the error transfer function of the CLOWFS system, as plotted in Fig. 13. The unity-gain frequency should be $f_1 = 1/(2\pi \times 7 \text{ s}) = 0.023 \text{ Hz}$, and the square root of the ratio of corrected to uncorrected power should be approximately (f/f_1) for $f < f_1$. More accurately, the error transfer function at all frequencies is calculated numerically for a 1.2 s integration of images on a 7 s iteration period, and delays smaller than $(7 \text{ s} - 1.2 \text{ s}) = 5.8 \text{ s}$. The match between the measured transfer functions and the expected transfer function (the colored lines compared to the black dashed line in Fig. 13) is quite good.

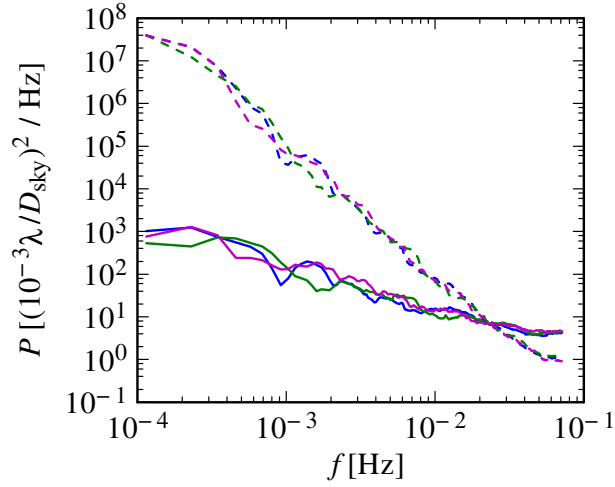


Fig. 12. Power spectral densities of Milestone 2 data runs, same data as in Figs. 10 and 11 with x and y powers summed. Solid lines are corrected and dashed lines are uncorrected. Blue is run #1, green is run #2, and magenta is run #3. The closed-loop unity-gain frequency of the correction with iterations separated by 7 s is expected *a priori* to be $1/(2\pi \times 7 \text{ s}) = 0.023 \text{ Hz}$, in excellent agreement with the measurements. The plot is smoothed as described in Appendix 1.

5.2. Calibration requirement

The calibration requirement takes two forms, first as a measurement of the mean residual after correction, and second as a measurement of uncorrected sinusoidal inputs.

The first requirement is that the magnitudes of mean x and mean y corrected measurements be less than

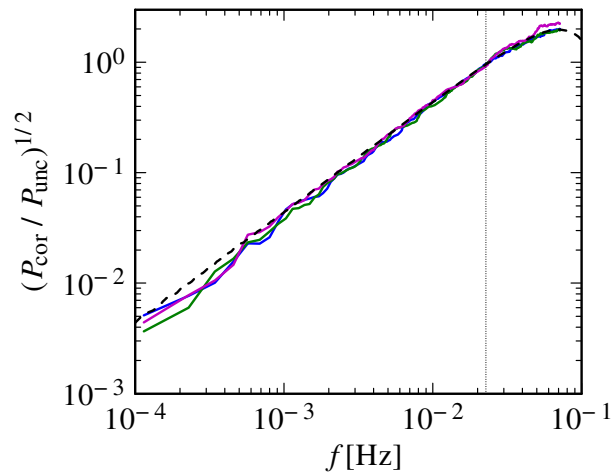


Fig. 13. Error transfer function. The three colored lines correspond to the square roots of the ratios of the colored lines in Fig. 12, the corrected power (solid lines in Fig. 12) divided by uncorrected power (dashed lines in Fig. 12), each smoothed as described in Appendix 1. The black vertical dotted line marks f_1 , where f_1 is the closed-loop unity-gain frequency. The black dashed line is a numeric expectation of the transfer function, for a loop operating with 1.2 s integrations per 7 s iteration.

$3 \times 10^{-3} \lambda D_{\text{sky}}$. The means of the corrected x and y measurements from the three runs (the data in Fig. 11) are $(\delta_x, \delta_y) = (-0.11, -0.09), (0.01, -0.08),$ and $(0.00, -0.13) \times 10^{-3} \lambda D_{\text{sky}}$, giving rms quadrature sums of x and y means of $\delta = 0.14, 0.08,$ and $0.13 \times 10^{-3} \lambda D_{\text{sky}}$, all well below the $3 \times 10^{-3} \lambda D_{\text{sky}}$ requirement. These are tabulated and summarized in the conclusions in Sec. 6.

The second requirement is that the amplitude of sinusoidal input signals be measured with errors below $3 \times 10^{-3} \lambda D_{\text{sky}}$. This test is performed using the same technique as the uncorrected measurement of disturbances described above, except that the disturbances are not a sequence of random variates selected from a nominal power spectral density, but are simply sinusoids. The amplitudes of the sinusoids were set at levels comparable to the corrected residuals. The x and y amplitudes were chosen based on equal voltages (70 mV), which come to slightly different λD_{sky} amplitudes (because of different piezo gains), $1.81 \times 10^{-3} \lambda D_{\text{sky}}$ for x and $1.91 \times 10^{-3} \lambda D_{\text{sky}}$ for y . Converting these sinusoidal amplitudes to rms amplitudes and adding them in quadrature yields $1.86 \times 10^{-3} \lambda D_{\text{sky}}$, about 75% larger than the rms measured corrected summed residuals σ of 1.07, 1.10, and $1.05 \times 10^{-3} \lambda D_{\text{sky}}$. The two sinusoids are applied simultaneously, with a 56 s period in x and 70 s period in y .

The calibration test is analyzed through the power spectral densities of the uncorrected measurements. These power spectral densities are shown in Fig. 14. These PSDs are calculated without the Nuttall window used in the other PSD analyses in this milestone, but rather with a “natural” equal-weighted (rectangular) window, to retain high spectral resolution. The data are not drift-subtracted as was done for Fig. 7, so the continuum levels are dominated at low frequencies by this (directional) drift term, but this continuum level is negligible at the sinusoidal input frequencies. The peaks in the two PSDs are large enough compared to the background power levels ($> \times 10^3$) that no subtraction is performed, the peak

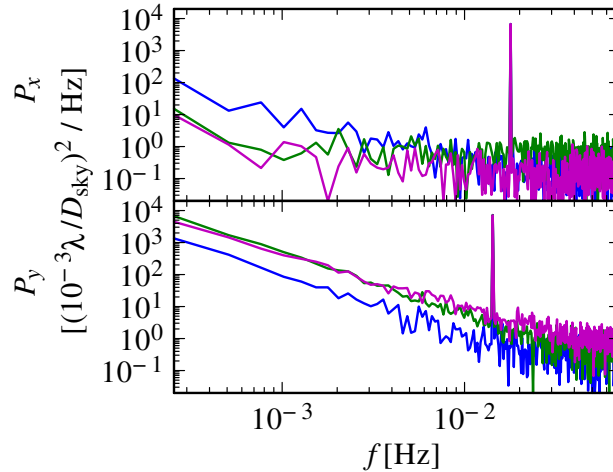


Fig. 14. Power spectral densities of Milestone 2 calibration verification runs. Blue is run #1, green is run #2, and magenta is run #3. The x and y actuators were driven with sinusoids of amplitudes $1.81 \times 10^{-3} \lambda D_{\text{sky}}$ and $1.91 \times 10^{-3} \lambda D_{\text{sky}}$, with periods of 56 and 70 s, respectively, in vacuum with no other disturbances added, and no corrections performed. Each peak has 10^3 - $10^4 \times$ the PSD of the continuum at nearby frequencies, so no attempt was made to subtract any “background” power. The rms difference between input and measured amplitudes is 1.7% for the 6 peak measurements (3 runs, 2 axes). This plot is not smoothed.

levels are simply integrated over one frequency bin to convert them into amplitudes. The x and y fractional errors in the measured amplitudes with respect to the amplitudes actually applied, for the 3 runs were (2.6%, 0.4%), (0.6%, 1.3%), and (2.6%, -0.7%). The rms quadrature sum of x and y for the three runs was 2.3%. The milestone calibration requirement is that the calibration error be below $3 \times 10^{-3} \lambda/D_{\text{sky}}$, while this experiment measures, for signals of comparable (slightly larger) amplitudes than on average, $\epsilon = 0.04 \times 10^{-3} \lambda/D_{\text{sky}}$, nearly two orders of magnitude below the requirement, for input levels higher than the corrected residuals.

6. CONCLUSIONS

This document describes the completion of the PIAA Milestone #2 requirements, demonstrating tip-tilt control at levels relevant to flight missions. The requirements are that tip-tilt be controlled to $10 \times 10^{-3} \lambda/D_{\text{sky}}$ rms over 1000 iterations, and that the calibration errors be below $3 \times 10^{-3} \lambda/D_{\text{sky}}$. These requirements must be met on each of three separate runs.

The results, as described in detail above, can be summarized as follows:

Run	correction requirement			calibration requirement					
	σ_x	σ_y	Require < 10	δ_x	δ_y	Require < 3	ϵ_x	ϵ_y	Require < 3
1	0.82	0.71	1.08	-0.11	-0.09	0.14	0.05	0.01	0.05
2	0.77	0.78	1.10	0.01	-0.08	0.08	0.01	0.02	0.03
3	0.69	0.80	1.06	0.00	-0.13	0.13	0.05	-0.01	0.05

Table 1. Milestone requirements and observed performance. The units for all measurements are $10^{-3} \lambda/D_{\text{sky}}$. The σ measurements are rms residuals after correction, δ are mean residuals, and ϵ are errors in sinusoidal measurements.

These results perform better than the milestone requirements by a large margin, between $9 \times$ and $100 \times$. For the correction and the mean residuals, this is in the presence of disturbances at rms levels near $90 \times 10^{-3} \lambda/D_{\text{sky}}$. The uncertainty in the scale factor determination, which is a systematic multiplication of every measured value presented in terms of λ/D_{sky} , is estimated at 3.6% (see Appendix 2), which introduces negligible changes to the interpretations of the margins by which these measurements exceeded the requirements. We claim that the tip-tilt milestone requirements have been met, with a substantial margin.

The CLOWFS, as implemented in this milestone report, is compatible with any coronagraph that uses an opaque focal plane mask to block starlight. This includes conventional Lyot type coronagraphs and band-limited Lyot coronagraphs, as well as most PIAA coronagraphs. The results described in this paper can be generalized to these coronagraphs.

A number of other coronagraphs use phase-shifting (non-absorbing) focal plane masks, such as the Vortex coronagraph, the 4 quadrant or 8 octant coronagraphs, and the PIAACMC. For these coronagraphs, the CLOWFS implementation is different: the Lyot mask after the focal plane mask is a mirror with a hole, reflecting the light that is outside the geometric pupil to the CLOWFS camera. The

coronagraph focal plane is re-imaged on the CLOWFS detector, which, for a perfect alignment, shows the same PSF as lands on the occulter, *i.e.*, the light rejected by the coronagraph is sent to the CLOWFS detector. The CLOWFS image is a linear function of tip and tilt, and the CLOWFS control loop can be identical to the control loop implemented for this milestone.

While this alternate ‘‘Lyot pickoff’’ implementation of the CLOWFS has been numerically simulated and is expected to yield the same precision as the implementation presented in this paper, it has never been tested in the laboratory. The results obtained for this milestone therefore cannot be considered to be applicable to these phase mask coronagraphs - experimental validation of the CLOWFS is thus needed for these coronagraphs.

The specific disturbances chosen to demonstrate the performance of the CLOWFS system do not have general significance, but the demonstrated error transfer function, as shown in Fig. 13, should be generally realizable for similarly constructed CLOWFS systems. This generality, at least for $f < f_1$, would hold provided that the system is adequately represented in a linear analysis. As described in Ref. 11 (e.g., Fig. 5 in Ref. 11), the level of nonlinearities in the CLOWFS response (due mostly to the annular occulter geometry) is expected to reach approximately 20% at displacements of $200 \times 10^{-3} \lambda / D_{\text{sky}}$. The closed-loop performance demonstrated in this report is well below those displacements (by $> 10^2 \times$), but these results should not be interpreted as validating performance in regimes where this constraint is violated.

Appendix 1. Power Spectral Densities

The calculations of power spectral densities in this experiment all begin with a temporal sequence of n real-valued measurements, taken at time intervals separated by Δt . For notation in this appendix, the measurements are denoted m_i with i ranging from 0 to $n-1$. By construction, this is a discrete sequence, and so discrete transforms will be used in the analysis.

When taking the Fourier Transform of the sequence m , one of two windows is applied. In cases where spectral resolution is less important than dynamic range (low sidelobes), a Nuttall 4-term continuous first derivative window [14] is applied,

$$w_i = a_0 + a_1 \cos(2\pi i/n) + a_2 \cos(4\pi i/n) + a_3 \cos(6\pi i/n)$$

$$a_0=0.355768, \quad a_1=-0.487396, \quad a_2=0.144232, \quad a_3=-0.012604$$

In cases where spectral resolution is more important than dynamic range, a rectangular (or top-hat) filter is applied,

$$w_i = 1$$

w_i is dimensionless in all cases.

In practice, all power spectral densities described in this document use the Nuttall window, except for the measurement of sinusoidal amplitudes to satisfy the calibration milestone requirements, as used in Fig. 14, which uses the rectangular window.

The power spectral densities reported here are one-sided power (*i.e.*, undefined for negative frequencies), and the zero-frequency result is not meaningful in any of these analyses, so for positive frequencies,

$$P_k = 2\Delta t |\sum_j m_j w_j e^{2\pi i j k / n}|^2 / (n \sum_j w_j^2),$$

for any k from 1 to $n/2-1$. The sums $\Sigma_j \dots$ are taken for $j=0$ to $j=n-1$, and P_k is interpreted as the power spectral density at frequency $f = k/(n\Delta t)$, and has dimensions of $[m]^2 / \text{Hz}$, where $[m]$ is the dimension of the measurements m_i .

All power spectral densities shown in this document are plotted on a log-log scale, and for every case except Fig. 14 (Fig. 14 contains the only PSD using a rectangular window, where spectral resolution is a priority), the plot shows the individual powers smoothed by a rolling average of fractional frequency width,

$$P_{k,\text{plot}} = \langle P_j \rangle \text{ for } 0.8k < j < 1.2k,$$

where $\langle \dots \rangle$ denotes a mean. At high frequencies, this reduces the noise inherent in the power spectral density calculations.

Appendix 2. Error Estimates

The errors relevant to this experiment are readily categorized as random and systematic errors. The random noise is estimated from the under-vacuum PSD with no corrections and no disturbances added (Fig. 8), while the systematic errors are estimated by the chain of errors in the individual components of the scaling constants S_x and S_y .

A2.1. Random errors

An estimate of the random errors comes from the shape of the power spectral density of uncorrected, undisturbed under-vacuum measurements as shown in Fig. 8. The high-frequency end of the PSD appears to be approaching an asymptotic value, which would be true for a white-noise component, as would be expected for any errors that are uncorrelated between CLOWFS images. These errors would most likely be shot noise in the signal and read noise in the detector. This random noise floor, corresponds approximately to $0.2 \times 10^{-3} \lambda D_{\text{sky}}$ rms, uncorrelated between measurements. This number is comfortably small so that further precision in the noise analysis is not warranted.

A2.2. Systematic errors

The dominant systematic noise source is in the determination of the scale factors S_x and S_y relating volts to λD_{sky} , as shown in Figs. 3 and 9, and described in detail in Secs. 3.5.2-3.5.4. This scale factor determination is performed once for the entire experiment, so errors in its determination will produce a uniform multiplicative error to every measurement that is later expressed in λD_{sky} .

A2.2.1. Errors in $S_{1,x}$ and $S_{1,y}$

The errors in $S_{1,x}$ and $S_{1,y}$ can be estimated by the rms residuals (bottom of Fig. 5), which are 0.02 pix rms (similar for each of x and y). A simplistic treatment (assuming uncorrelated errors) would say that the amplitude measurements (top of Fig. 5) of ~ 0.8 pix, over 625 samples, would see a contribution of $0.02 \text{ pix}/(625)^{1/2} \sim 10^{-3}$ pix, for a relative error on the order of 0.1%. To be clear, this is the contribution of random errors, assumed uncorrelated, to the measurement of the centroid sinusoidal amplitude at the science camera. This relative error is much smaller than those of S_2 and S_3 .

A2.2.2. Errors in S_2

The error in S_2 , from camera pixels to microns at the occulter, is estimated from the results of moving the occulter and PSF together, and equating the pixel motion on the camera with the encoder motion at the occulter. The occulter encoder registered a 67.5 micron move, while the science camera image moved by 12.9 pixels, giving a measurement of 5.23 microns/pix. This differs by 0.6% from the nominal values in Sec. 3.5.3 of 5.2 microns/pix, which was used in the analysis. The accuracies of the two numbers involved were 0.25 microns at the occulter and 0.1 pix at the camera for each of the two locations that were differenced. An overly conservative treatment would say that an uncertainty of 0.5 microns (twice the individual error) out of 67.5, and 0.2 pix out of 12.9 together give a 1.7% relative uncertainty. The difference between the measured and assumed values is well within this (0.6%), but a conservative treatment would assume that 1.7% is an upper limit to the uncertainty in this step of the scaling.

A2.2.3. Errors in S_3

The estimation of errors in S_3 is broken into two different measurements. The measurement of f/D at the science camera is done by establishing the distance from the source image plane to the pupil image plane using the encoders on the camera stage, 228.5 mm, which itself needs no error bars because the pupil diameter measurement scales with errors in this number. The pupil diameter is $427 \text{ pix} \pm 4 \text{ pix}$ (it has an irregular edge), for a relative uncertainty of 1%. Using the specified CCD pixel size of $13 \mu\text{m}$, and the laser wavelength of 808 nm, $f\lambda/D = 33.2 \mu\text{m}$ at the camera. The magnification from the camera to the occulter is 2.5 (as implicitly verified in the second step of the scale factor determination, described in the previous paragraph), giving $f\lambda/D = 13.3 \mu\text{m}$ at the occulter, with an uncertainty of approximately 1%. The additional measurement needed to verify the relationship between microns at the occulter and λ/D_{sky} is the PIAA off-axis magnification M . One unresolved ambiguity in the available measurements is the magnification in the absence of the PIAA optics, between the source and the occulter. Without having independent measure of this, a mismatch in the expected 1:1 match in input and output focal lengths of the M1 and M2 PIAA mirrors would be interpreted here as a change in off-axis magnification. Without any reason to believe that there would be an anticorrelation between these errors, attributing all of the measured error to only the off-axis magnification should be a conservative treatment. Referencing all measurements to distances at the occulter (again using the prior scale factors), the relative mismatch between the expected and measured off-axis magnification is 2.7%. Coupled with the 1% uncertainty in the $f\lambda/D$ determination, the total uncertainty in the third step is 2.9%.

A2.2.4. Total systematic errors

Taking the systematic uncertainties of S_1 , S_2 , and S_3 (of which the errors in S_1 are negligible) together in quadrature, the total uncertainty in the scale factor S_x and S_y determination is 3.4% (approximately the same in both axes). A summary of these errors appears in Table 2.

	nominal value	measured value	uncertainty	origin of uncertainty
$S_{1,x}$ and $S_{1,y}$	use measured	(0.80, 0.84) pix / 5 V	0.1%	residuals to fit
S_2	5.21 $\mu\text{m}/\text{pix}$	5.23 $\mu\text{m}/\text{pix}$	1.7%	accuracy of meas. values
S_3	$(\lambda/D_{\text{sky}}) / (33.3 \mu\text{m})$	$(\lambda/D_{\text{sky}}) / (33.4 \mu\text{m})$	2.9%	accuracy of meas. values

Table 2. Scale factor values, both nominal and measured, and their estimated uncertainties.

REFERENCES

- [1] Guyon, O. 2003, "Phase-induced amplitude apodization of telescope pupils for extrasolar terrestrial planet imaging," *A&A* **404**, 379-387.
- [2] Traub, W.A.; Vanderbei, R.J. 2003, "Two-Mirror Apodization for High-Contrast Imaging," *ApJ*, **599**, 695-701.
- [3] Vanderbei, R.J.; Traub, W.A. 2005, "Pupil Mapping in Two Dimensions for High-Contrast Imaging," *ApJ* **626**, 1079-1090.
- [4] Guyon, O., Pluzhnik, E.A., Galicher, R., Martinache, F., Ridgway, S.T., Woodruff, R.A. 2005, "Exoplanet Imaging with a Phase-induced Amplitude Apodization Coronagraph. I. Principle," *ApJ* **622**, 744-758.
- [5] Martinache, F., Guyon, O., Pluzhnik, E.A., Galicher, R., Ridgway, S.T. 2006, "Exoplanet Imaging with a Phase-Induced Amplitude Apodization Coronagraph. II. Performance," *ApJ* **639**, 1129-1137.
- [6] Vanderbei, R.J. 2006, "Diffraction Analysis of Two-dimensional Pupil Mapping for High-Contrast Imaging," *ApJ* **636**, 528.
- [7] Pluzhnik, E.A., Guyon, O., Ridgway, S.T., Martinache, F., Woodruff, R.A., Blain, C., Galicher, R. 2006, "Exoplanet Imaging with a Phase-Induced Amplitude Apodization Coronagraph. III. Diffraction Effects and Coronagraph Design," *ApJ* **644**, 1246-1257.
- [8] Guyon, O., Pluzhnik, E.A., Kuchner, M.J., Collins, B., Ridgway, S.T. 2006, "Theoretical Limits on Extrasolar Terrestrial Planet Detection with Coronagraphs", *ApJSS* **167**, 81-99.
- [9] Lozi, J., Martinache, F., Guyon, O. 2009, "Phase-Induced Amplitude Apodization on centrally obscured pupils: design and first laboratory demonstration for the Subaru Telescope pupil," *PASP* **121**, 1232-1244.
- [10] Guyon, O., Martinache, F., Belikov, R., Soummer, R. 2010, "High Performance PIAA Coronagraphy with Complex Amplitude Focal Plane Masks," *ApJ* **192**, 220-232.
- [11] Guyon, O., Matsuo, T., Angel, R. 2009, "Coronagraphic Low Order Wavefront Sensor: Principle and Application to a Phase-Induced Amplitude Coronagraph," *ApJ* **693**, 75-84.
- [12] Kern, B., Give'on, A., Kuhnert, A., Levine-West, M.B., McMichael, I., Moody, D.C., Niessner, A.F., Pueyo, L., Shaklan, S.B., Traub, W.A., Trauger, J.T., Belikov, R., Guyon, O. 2009, "Phase-induced amplitude apodization (PIAA) coronagraph testing at the High Contrast Imaging Testbed," *Proc. SPIE* **7440**, 74400H.
- [13] Kern, B., Give'on, A., Kuhnert, A., Niessner, A., Guyon, O. 2011, "Laboratory testing of a Phase-Induced Amplitude Apodization (PIAA) coronagraph," *Proc. SPIE* **8151**, 815104.
- [14] Nuttall, A.H. 1981, "Some Windows with Very Good Sidelobe Behavior," *IEEE Trans. Acoust., Speech, Signal Process.*, **ASSP-29**, 84-91.